ADVANCED FUNCTIONAL MATERIALS
www.afm-journal.de

Patterned Assembly of Transition Metal Dichalcogenide/Graphene Heterostructures via Direct Laser Writing

Xin Chen, Stefan Wolff, Sofiia Zuieva, Robert Schusterbauer, Rida Shaikh, Christian E. Halbig, Anton Habel, Roland Gillen, Kathrin C. Knirsch, Ievgen Donskyi, Siegfried Eigler, Janina Maultzsch, and Andreas Hirsch*

Connecting two-dimensional (2D) material layers via interface linkers represents a new avenue for fabricating 2D heterostructures. Utilizing light to remotely modulate this interface function allows for seamless assembly and patterning in a single run. Here, an efficient method for fabricating patterned 2D heterostructures using direct laser writing is demonstrated, drawing a conceptual parallel to laser printing. In the approach, functionalized transition metal dichalcogenide (TMD) dispersions serve as inks, graphene as the substrate, and a Raman laser as the patterning tool. Unlike laser printing's electrostatic interactions, the method achieves patterned assembly through covalent bonding between TMDs and graphene. Selective Raman laser irradiation of functionalized TMD/graphene heterostructures triggers localized reactions, forming chemically modified domains exclusively in the laser-irradiated regions, as confirmed by Raman spectroscopy, Kelvin probe force microscopy (KPFM), and time-of-flight secondary ion mass spectrometry (ToF-SIMS). Experimental and theoretical analyses of the interface composition and structure provide new insights into laser-induced chemistry. The work demonstrates the potential for high-throughput assembly of customizable 2D heterostructures, with enhanced compatibility for subsequent patterning through photolabile linkers and photoinduced coupling. Additionally, the results provide deeper insights into chemistry within confined 2D spaces, offering a novel approach to nanoscale heterostructure engineering.

1. Introduction

Vertically stacking different two-dimensional (2D) material layers into heterostructures has emerged as an appealing strategy to engineer the properties of 2D materials, explore unconventional physical phenomena, and fabricate novel devices. This strategy has been the catalyst for a new era of nanomaterial design with significant tunability. In particular, the choice of 2D materials, stacking order, stacking configuration, number of layers, as well as the interlayer distance are found to be crucial for the properties of heterostructures.[1] Adjusting even just one of these factors can significantly impact the properties of the heterostructures as a whole.[2,3] In the past 10 years, remarkable progress has been made in the preparation of van der Waals (vdW) heterostructures with different band alignments, stacking orders, and twist angles.[4] These assemblies are usually achieved via mechanical stacking, epitaxial growth, or chemical vapor deposition (CVD).[5] However, these

X. Chen, S. Zuieva, R. Schusterbauer, C. E. Halbig, A. Habel, I. Donskyi, S. Eigler
Institute of Chemistry and Biochemistry
Freie Universität Berlin
Altensteinstraße 23a, 14195 Berlin, Germany
E-mail: xin.chen@fu-berlin.de

The ORCID identification number(s) for the author(s) of this article can be found under https://doi.org/10.1002/adfm.202425776

DOI: 10.1002/adfm.202425776

S. Wolff, R. Gillen, J. Maultzsch
Department of Physics
Friedrich-Alexander-Universität Erlangen-Nürnberg
Staudtstraße 7, 91058 Erlangen, Germany

R. Shaikh, K. C. Knirsch, A. Hirsch
Department of Chemistry and Pharmacy
Friedrich-Alexander-Universität Erlangen-Nürnberg
Nikolaus-Fiebiger-Straße 10, 91058 Erlangen, Germany

methods often rely on expensive instrumentation and delicate control of reaction conditions, which limits time and cost efficiency. Additionally, the quality, tunability, and compatibility of the resulting vdW heterostructures with subsequent patterning processes remain challenging.

Drawing inspiration from natural cross-linking processes, a few research groups have embarked on using molecular crosslinkers to connect 2D building blocks, thus creating covalently linked heterostructures. For example, Ippolito et al. demonstrated the covalent conjugation of deposited molybdenum disulfide (MoS_2) nanosheets using dithiols, leading to a reproducible enhancement in field-effect mobility, current ratio, and switching time in liquid-gated transistors.[6] Mechanical tests showed that the interface linking can also increase the mechanical resistance to the lateral motion, without altering the compressive modulus or generating strain.[7] Vázquez Sulleiro et al. fabricated a MoS_2/graphene field-effect transistor device by covalently coupling MoS_2 nanosheets to a graphene film (denoted as G) through a molecular crosslinker, which bears one maleimide end and one diazonium end.[8] However, the homogeneity of their heterostructures is compromised by the random accumulation of MoS_2 flakes on the graphene surface, posing challenges for further patterning and integration into a high-performance device. In a recent study, we showcased a novel bottom-up approach for fabricating and patterning high-quality G/MoS_2 heterostructures.[9] This method involves the use of heterobifunctional linkers with a diazonium end and a photolabile halogen end. The incorporation of photolabile linkers facilitates remote and efficient initiation and control of covalent interface assembly. This interface coupling, combined with the utilization of a pre-patterned bottom layer, enables the precise transduction of both chemical information and topographic patterns from the bottom to the top layer of the heterostructures.

Creating the aforementioned patterned heterostructures still requires a pre-patterned bottom material layer, involving a multi-step lithography-assisted fabrication process. To mitigate the challenges associated with electron-beam lithography (EBL) process, here, we present a mask-free, reproducible, and efficient approach to fabricate covalently linked and patterned heterostructures. The functionalized transition metal dichalcogenides (fun-TMDs, where TMD = MoS_2, WS_2, $MoSe_2$) with surface tethered photolabile linkers will be initially prepared as the material inks. These inks will then be deposited as a thin film on top of CVD-grown G, in analogy to toner being attached to a drum in the laser printing process. The focused Raman laser beam is directed at specific positions on the material stacks, triggering chemical reactions in the photolabile linkers at these targeted spots. As the laser scans the sample surface along a predefined path, these localized reactions selectively modify certain areas. This selective exposure to electromagnetic radiation results in a patterned structure, featuring spatially defined chemically modified regions and non-modified domains. Compared to lithography, this direct laser writing approach significantly reduces the fabrication cost and time, which makes the patterned heterostructures widely accessible.[10] Our approach unlocks the potential of functionalized material inks as 2D synthons for the construction of patterned 2D heterostructures on desired substrates. This development opens the door to a myriad of novel 2D and three-dimensional (3D) nanoarchitectures for applications in electronic, sensing, and catalytic devices.

2. Results and Discussion

2.1. Fabrication and Characterization of Patterned TMD/G Heterostructures

The fabrication of patterned TMD/G heterostructures entails three main steps (**Figure 1**): 1) preparation of fun-TMD inks, 2) deposition of fun-TMDs on top of G, and 3) laser writing and reading. First, the fun-TMD inks were prepared according to our reported protocol by reacting chemically exfoliated TMD nanosheets (ce-TMDs) with 4-iodobenzendiazonium salt.[11] The resulting fun-TMDs were characterized by zeta potential, Raman spectroscopy, and thermogravimetric analysis (TGA) (Figures S1–S2 and Table S1, Supporting Information). In the second step, these functionalized TMD nanosheets were assembled into a thin layer at the toluene-water interface through a modified Langmuir-Blodgett (LB) method.[12] Upon toluene evaporation, the pre-assembled fun-TMD layer was transferred onto the top of a G film, forming a fun-TMD/G heterostructure (Figure S3, Supporting Information). A subsequent writing-reading cycle of Raman irradiation was implemented. During the writing scan, Raman spatial mapping (point by point, with a step size of 1 μm) was conducted in a defined raster pattern (green block in Figure 1b), utilizing a high laser power (12-17 mW). This process induces photochemical reactions at the specified spots across the entire mapped area (5×5 μm^2, unless indicated otherwise). The follow-up scan, employing a relatively lower laser power (2 or 7 mW) over a broader area, facilitated the readout of the generated pattern.

The fabrication process was monitored through Raman spectroscopy. Using the MoS_2-based system as an example, a comparison of the Raman spectra of fun-MoS_2 and ce-MoS_2 reveals a new broad band with two most intense peaks (indicated by red dots in **Figure 2a**) at 1379 and 1585 cm^{-1} for fun-MoS_2, which can be attributed to the functional groups.[13] The Raman spectra of fun-MoS_2/G display characteristic modes from both fun-MoS_2 ($E^1{}_{2g}$ and A_{1g}, indicated by orange dots in Figure 2a) and graphene (G and 2D, indicated by blue dots in Figure 2a), with a notable overlap between the functional group-related bands and the G- (and D-) bands of the graphene film. Importantly, the Raman spectrum of fun-MoS_2/G recorded under the writing condition shows a more pronounced increase in D-band intensity, a less intense 2D-band, and broader G- and 2D-bands compared to pristine graphene and fun-MoS_2/G under the reading condition. This suggests that the graphene film in fun-MoS_2/G was more defective upon the higher laser power irradiation (writing condition).[14] The formation of these defects (discussed in detail below) depended on the employed laser power and was likely a result of photo/thermal induced reactions. See Table S2 (Supporting Information) for detailed information on peak positions and full width at half maximum (FWHM).

To systematically analyze the effect of the laser power on the Raman spectra of fun-MoS_2/G and the interactions between fun-MoS_2 and graphene, we monitored the Raman evolution of both fun-MoS_2/G and reference fun-MoS_2 with increasing laser power. As the laser power increases, the Raman spectra

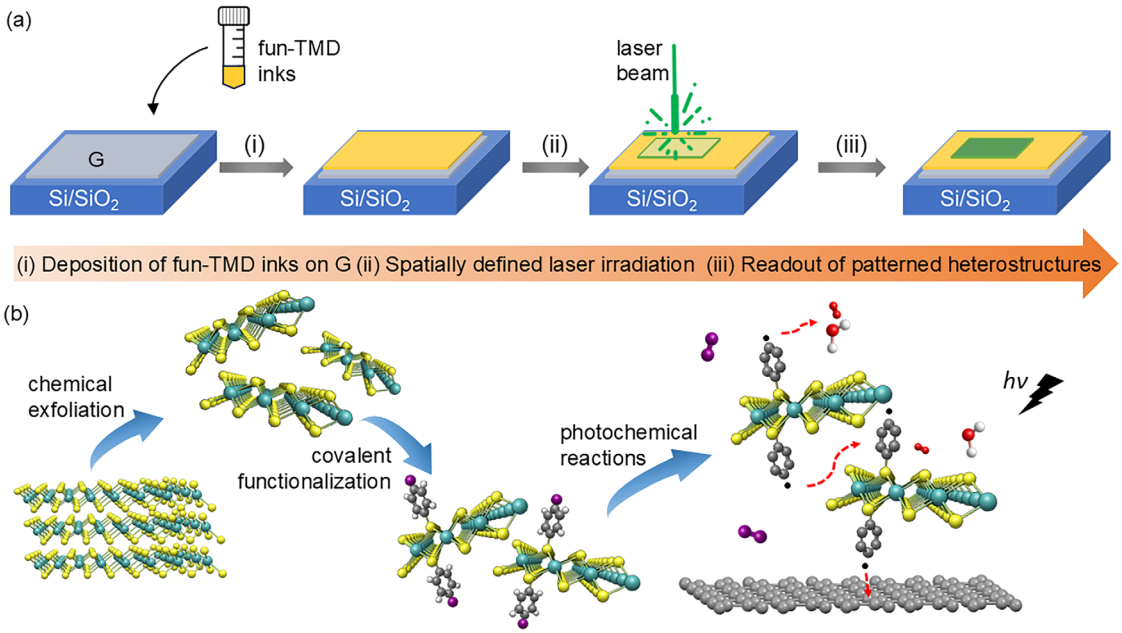

Figure 1. a) 2 fabricating patterned TMD/G heterostructures on a Si/SiO_2 substrate. The gray and yellow plates represent CVD-grown graphene and the deposited fun-TMD layer, respectively, while the green block pattern indicates the photochemically modified domain created by direct laser writing. b) Illustration of major chemical processes in (a): Chemical exfoliation of bulk MoS_2 powder produces monolayer-rich TMD nanosheets (ce-TMDs) dispersed in water. Covalent functionalization of ce-TMDs with diazonium salts forms functionalized TMDs (fun-TMDs), with 4-iodophenyl groups tethered to the basal plane. Upon laser irradiation of fun-TMD/graphene stacks, photochemical reactions such as deiodination and phenyl radical formation may occur. These radicals can then undergo a series of reactions with surrounding materials or chemical species (red dashed arrows), leading to photochemically modified heterostructure domains exclusively in the irradiated areas. Atoms are displayed as follows: white for H, gray for C, red for O, yellow for S/Se, cyan for Mo/W, and purple for I.

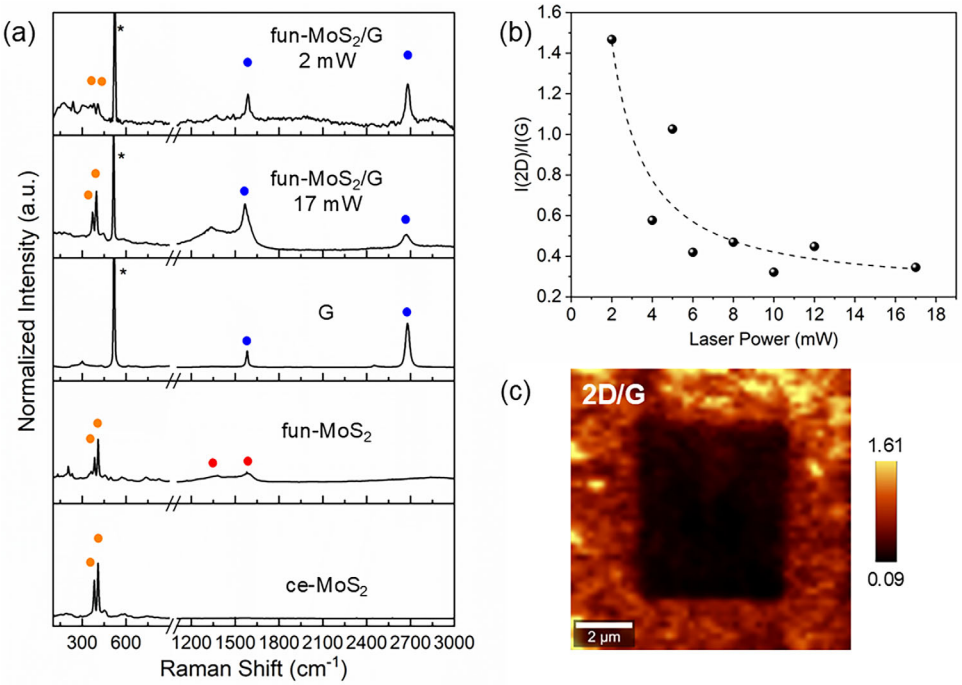

Figure 2. a) Raman spectra (λ_{ex} = 532 nm) of ce-MoS_2, fun-MoS_2, pristine G, and fun-MoS_2/G (measured at 17 and 2 mW). The Raman intensities of ce-MoS_2, fun-MoS_2, and fun-MoS_2/G are normalized to the intensity of the E^1_{2g} mode. Orange, blue, and red dots mark MoS_2, graphene, and functional group-related peaks. The asterisk labels the Raman peaks that correspond to the silicon substrate. b) I(2D)/I(G) ratio of fun-MoS_2/G as a function of laser power, with a dashed trendline for guidance. c) Raman I(2D)/I(G) map of patterned fun-MoS_2/G (λ_{ex} = 532 nm, laser power = 7 mW), showing photochemically modified regions with lower I(2D)/I(G) ratios.

of fun-MoS_2/G (Figure S4a, Supporting Information) display an increased intensity of the D-band, a decreased intensity of the 2D-band, and broadening of the D-, G-, and 2D-bands. These trends can be more clearly identified through the plots of peak intensity ratios, I(2D)/I(G) (Figure 2b) and I(D)/I(G) (Figure S4f, Supporting Information), along with the FWHM of the G- and 2D-bands (Figure S4c,e, Supporting Information), as a function of laser power. Critically, due to the significant overlap between the functional group-related bands and the D- and G-band of graphene, the increased spectral intensity in this region cannot be attributed solely to defect formation in the graphene (Figure S5b, Supporting Information). Therefore, the Raman peak intensity ratio I(D)/I(G) cannot be used to estimate the degree of functionalization in this case. Nevertheless, the change in 2D-band intensity is most likely related to alterations in the graphene lattice, making it a reliable indicator of defect formation in graphene.

The I(2D)/I(G) ratio is inversely related to the defect density of graphene.[15,16] Employing higher laser power results in a decrease in the I(2D)/I(G) values, thereby increasing the defect density until a laser power of 10 mW, at which point a saturation is reached (Figure 2b). After reaching the saturation point, the defect density remains at a plateau, irrespective of further increases in laser power. Such a trend underscores that the defect generation in graphene is initially energy-limited and then may become reactant-limited. This suggests that these defects likely arise from sp^3-hybridized carbon atoms formed through covalent coupling of graphene with photogenerated phenyl radicals in fun-MoS_2, rather than graphene oxidation. These radicals are produced by photon-induced dehalogenation, making their quantity energy-dependent. The limited number of photolabile functional groups in fun-MoS_2 could explain the saturation of the reaction rate once all groups are fully activated and have reacted.

Analysis of the G- and 2D-band positions (Pos(G) and Pos(2D)) (Figure S4b,d, Supporting Information) and their intensity ratios (I(G)/I(2D)) (Figure S4g, Supporting Information) under varying laser powers reveals that Pos(G) remains constant, while Pos(2D) shifts downward as laser power increases. This downshift, also observed with an increasing number of graphene layers, along with the rise in I(G)/I(2D) from 0.5 to 3.5, suggests enhanced interactions between graphene and fun-MoS_2.[17,18] Such strengthened interactions are presumably attributed to the covalent coupling of fun-MoS_2 to graphene as postulated above. In addition, peaks corresponding to molybdenum dioxide (MoO_2) and molybdenum trioxide (MoO_3) (Figure S5a, Supporting Information) were detected in the Raman spectra of fun-MoS_2. These peaks became more prominent when higher laser power was used, indicating the oxidation of MoS_2, a phenomenon discussed in detail in our earlier study.[19] Interestingly, when a 23.1 mW Raman laser was applied, the functional group-related peaks in the 1300–1600 cm^{-1} range disappeared (Figure S5b and Table S3, Supporting Information). This suggests that the surface-tethered functional groups can be removed (de-functionalization) due to the high laser power irradiation.

Building on the correlation between Raman laser power and interface properties, we utilized 12 mW laser power to directly write chemically modified MoS_2/G heterostructure domains, aiming for a high degree of graphene functionalization and enhanced contrast in Raman mapping. The pattern read out using a 7 mW laser power scan is shown in the Raman mapping (Figure 2c). Darker regions with lower I(2D)/I(G) ratios indicate areas with higher graphene defect density, because of a stronger covalent interface coupling. This pattern precisely matches the location and size of the input design, demonstrating an accurate method for spatially modifying heterostructures and interfaces.

The surface topography and electronic properties of the patterned MoS_2/G heterostructures were characterized using atomic force microscopy (AFM) and Kelvin probe force microscopy (KPFM) under ambient conditions. A large rectangular pattern, measuring 10 × 10 μm^2, was fabricated using direct laser writing. The AFM image (**Figure 3a**) clearly shows the boundary between the highly irradiated region and the non-irradiated region, marked by a dashed line. The surface potential map (Figure 3b) reveals a distinct block pattern, where areas irradiated with higher laser power exhibit a slightly lower potential compared to surrounding regions. The maximum potential difference observed is ≈0.24 V. The alteration in surface potential was likely influenced by changes in local structures resulting from laser induced reactions at the surfaces and interfaces. By adopting this laser writing strategy, we also generated patterned tungsten disulfide/graphene (WS_2/G) and molybdenum diselenide/graphene ($MoSe_2$/G) heterostructures (Figures S6–S9, Supporting Information).

2.2. Probing Laser-Induced Chemical Changes in Heterostructures

To investigate changes in chemical composition and better understand the chemical events triggered by laser irradiation in fun-MoS_2/G, we characterized both non-irradiated and high-power laser (writing laser)-irradiated fun-MoS_2/G using time-of-flight secondary ion mass spectrometry (ToF-SIMS) and X-ray photoelectron spectroscopy (XPS). For this analysis, specialized fun-MoS_2/G heterostructures with irradiated domains up to 300 × 300 μm^2 were prepared. Comparing the XPS survey spectra of irradiated and non-irradiated regions reveals two additional peaks at 619.3 and 630.8 eV in the non-irradiated region (**Figure 4a**), corresponding to the iodine $3d_{5/2}$ and I $3d_{3/2}$ signals. The detection of iodine in the non-irradiated region confirms the presence of iodophenyl functional groups in fun-MoS_2. In contrast, the absence of iodine in the irradiated region suggests that laser irradiation led to deiodination, with the cleaved iodine likely removed through sublimation. The C *1s* core-level spectrum of non-irradiated can be deconvoluted into four major components (Figure 4b): C—C and C=C (284.5 eV), C—OH (285.2 eV), C—O—C (286.5 eV), and C=O (288.7 eV). The C—C and C=C species primarily originate from graphene and the phenyl-related functional groups, while the oxygen-containing species are likely due to adventitious carbon species, such as adsorbed CO, CO_2, or short-chain hydrocarbons.[20] Compared to the non-irradiated region, the irradiated area shows a significant increase in the C—OH contribution, indicating the formation of new species containing C—OH moieties as a result of laser irradiation.

The spatial distribution of the chemical composition in both non-irradiated and irradiated regions of fun-MoS_2/G were analyzed using spatially resolved ToF-SIMS. The laser-written patterns appear as greenish areas in Figure 4c. The chemical maps within the red block region are shown in Figure 4d–f, and the

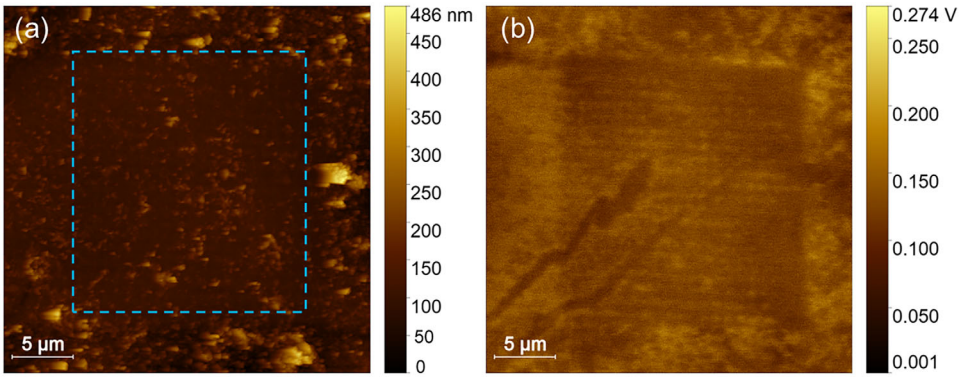

Figure 3. a) AFM image of patterned MoS_2/G heterostructures. The blue dashed block indicates the location of highly irradiated region. b) KPFM image of patterned MoS_2/G heterostructures.

negative ion spectra are presented in Figure S10 (Supporting Information). Both regions exhibit intense signals from MoS_2 (Figure 4d), indicating a relatively even distribution of fun-MoS_2 across both the intact and irradiated areas. Notably, the intensity maps of O^- and OH^- ions reveal a distinct contrast between the non-irradiated and irradiated regions, with significantly higher intensities detected primarily in the irradiated regions. The higher intensity of O^- signal in the irradiated region is likely due to the generation of MoO_x (x = 2 or 3) upon laser irradiation. The laser-induced oxidation of MoS_2 was also observed in our laser power-dependent Raman study of fun-MoS_2 (Figure S5, Supporting Information).[19] The dense accumulation of OH^- ions in the irradiated region (Figure 4f), which is not present in the functional groups of fun-MoS_2, is likely introduced during the laser-writing process. These OH species are presumed to exist as phenol (C_6H_5OH) moieties, formed through the oxidation of surface-tethered phenyl radicals. This is supported by the increased content of C—OH species observed in Figure 4b.

Our experimental findings highlight the absence of an iodine signal in the XPS elemental survey of the irradiated areas, confirming that laser irradiation induced the deiodination of the functional groups in fun-MoS_2. This C—I bond cleavage may occur either homolytically,[21] generating reactive phenyl and iodine radicals that can recombine into iodine, or through photoinduced electron transfer (PET) from MoS_2 to iodophenyl groups, resulting in the formation of radical anions.[22] These radical anions can then break down into phenyl radicals and iodide ions. The highly reactive surface-tethered phenyl radicals in fun-MoS_2 can either bind to the underlying graphene layer or be oxidized to phenol in the presence of water and oxygen.

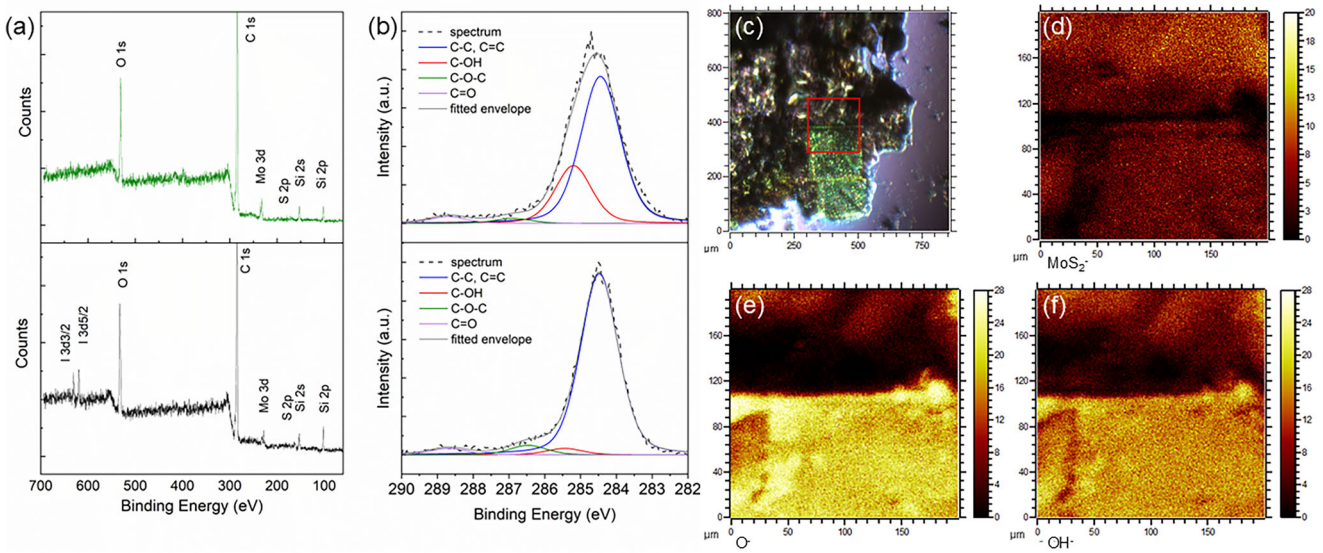

Figure 4. a) XPS survey spectra and b) C *1s* core level spectra of non-irradiated (bottom) and irradiated (top) regions of fun-MoS_2/G heterostructures. The C *1s* spectra are deconvoluted using a Lorentzian function. c) Optical image of the patterned MoS_2/G heterostructures, where fun-MoS_2 appears as the black layer, and the transparent graphene beneath shows a slight blue reflection. Green areas indicate laser-written patterns, while the red dashed box highlights the ToF-SIMS mapping area, comparing the non-irradiated (upper) and irradiated (lower) regions. d–f) High-resolution ToF-SIMS intensity maps (negative mode) of MoS_2^-, O^-, and OH^- secondary ions on the surface of fun-MoS_2/G, with O^- and OH^- signals predominantly detected in the irradiated region. The color scales in (d–f) represent intensity in counts.

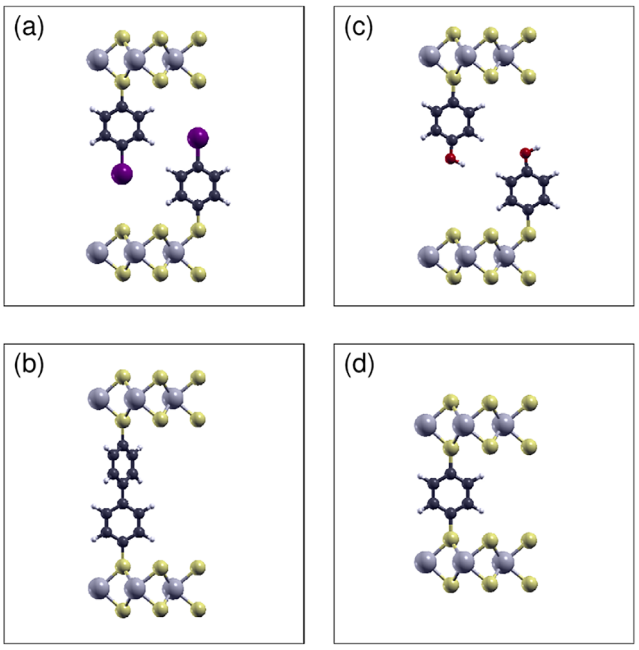

Figure 5. Relaxed structures of I-Ph-2MoS$_2$ a), BPh-2MoS$_2$ b), OH-Ph-2MoS$_2$ c), and Ph-2MoS$_2$ d). The atoms are displayed as follows: white for H, black for C, red for O, yellow for S, gray for Mo, and purple for I. For motifs (a,c), the functional groups must be positioned as far apart as possible; otherwise, functionalization on sulfur atoms with the same coordinates within the MoS$_2$ plane would necessitate a significant increase in the interlayer distance.

2.3. Density Functional Theory (DFT) Calculations

To get further insights into the interface structures and reaction pathways in fun-MoS$_2$ after laser irradiation, DFT calculations were conducted. We propose three pathways that the phenyl radicals might take at the interface of iodophenyl functionalized MoS$_2$: 1) coupling between phenyl radicals on neighboring nanosheets to form biphenyl linkages, 2) reaction with hydroxyl radicals (·OH), likely generated through peroxidase-like TMD-catalyzed reactions with water and O$_2$,[23] to form phenols, or 3) interaction with available sites on adjacent MoS$_2$ nanosheets. Relaxed structures of iodophenyl-functionalized MoS$_2$ (I-Ph-2MoS$_2$) and potential products of these three pathways: biphenyl linked MoS$_2$ layers (BPh-2MoS$_2$), phenol-functionalized MoS$_2$ (OH-Ph-2MoS$_2$), and phenyl linked MoS$_2$ (Ph-2MoS$_2$) were obtained using two 2 × 2 MoS$_2$ supercells, with functional groups placed between the layers (**Figure 5**). To simulate the experimental degree of functionalization (33 ± 1%, Table S1, Supporting Information), one of the four sulfur atoms participates in the functionalization, corresponding to a surface coverage of 25% in I-Ph-2MoS$_2$, BPh-2MoS$_2$ and OH-Ph-2MoS$_2$. To incorporate the same amount of phenyl, the surface coverage in Ph-2MoS$_2$ would need to be increased to 50%, which exceeds the maximum value observed in the experiment. The average interlayer distances between Mo atoms from adjacent layers are 14.1, 14.8, and 9.7 Å for BPh-2MoS$_2$, OH-Ph-2MoS$_2$, and Ph-2MoS$_2$, respectively (values are obtained via DFT calculations using the Perdew–Burke–Ernzerhof (PBE) exchange-correlation functional,[24] see Table S4 for more details, Supporting Information). The significant geometric discrepancies between Ph-2MoS$_2$ and the other two motifs suggest that it is less likely for a MoS$_2$ bilayer to accommodate both Ph-2MoS$_2$ and either BPh-2MoS$_2$ or OH-Ph-2MoS$_2$ simultaneously.

A comparison of the total energy difference per atom for the relaxed structures (Figure S11, Supporting Information) indicates that OH-Ph-2MoS$_2$ is the most stable motif, since it exhibits the lowest total energy per atom, followed by BPh-2MoS$_2$. The total energy per atom of Ph-2MoS$_2$ is even higher than the total energy per atom of I-Ph-2MoS$_2$, which makes the formation of Ph-2MoS$_2$ very unlikely. This suggests that BPh-2MoS$_2$ or OH-Ph-2MoS$_2$ are likely to form via pathways (1) and (2), respectively.

The reaction energy of pathway (1), calculated by subtracting the energy of I-Ph-2MoS$_2$ ($E_{\mathrm{I-Ph-2MoS_2}}$) from the energy of BPh-2MoS$_2$ ($E_{\mathrm{BPh-2MoS_2}}$) and the energy of an I$_2$ molecule ($E_{\mathrm{I_2}}$), is found to be -1.7 eV (Equation 1).

$$E_{R1} = [\,E_{\mathrm{BPh-2MoS_2}} + E_{\mathrm{I_2}}] - E_{\mathrm{I-Ph-2MoS_2}} \quad (1)$$

The reaction energy of pathway (2), calculated by subtracting the energy of I-Ph-2MoS$_2$ ($E_{\mathrm{I-Ph-2MoS_2}}$), half of the energy of an O$_2$ molecule ($E_{\mathrm{O_2}}$), and the energy of a water molecule ($E_{\mathrm{H_2O}}$) from the sum of the energy of OH-Ph-2MoS$_2$ ($E_{\mathrm{OH-Ph-2MoS_2}}$) and an I$_2$ molecule ($E_{\mathrm{I_2}}$), is -3.7 eV (Equation 2).

$$E_{R2} = \left[E_{\mathrm{OH-Ph-2MoS_2}} + E_{\mathrm{I_2}}\right] - \left[\,E_{\mathrm{I-Ph-2MoS_2}} + 1/2 \times E_{\mathrm{O_2}} + E_{\mathrm{H_2O}}\right] \quad (2)$$

This indicates that the formation of OH-Ph-2MoS$_2$ is thermodynamically favored compared to the formation of BPh-2MoS$_2$ and is in good agreement with our ToF-SIMs observations, in which OH species are predominantly distributed in the photochemically modified regions. Other, less likely, reaction pathways may lead to significant changes in the reaction energies, see Figure S11 (Supporting Information).

To further explore the potential formation of biphenyl-linked and phenol-functionalized MoS$_2$ in the laser irradiation process, phonon mode calculations were conducted on isolated iodobenzene, biphenyl, and phenol molecules, as well as the functionalized motifs (Figures S12–S14, Supporting Information): I-Ph-MoS$_2$, BPh-2MoS$_2$, and OH-Ph-MoS$_2$. Since the experimentally obtained Raman spectra of fun-MoS$_2$ exhibit a broad band in the range of 1000–1600 cm^{-1} (Figure 2a; Figures S1a and S5b, Supporting Information), which is absent in ce-MoS$_2$, we focused on investigating the phonon modes in this range for the relaxed structures. Compared to the isolated molecules, the corresponding phonon modes of the functionalized motifs are downshifted, which is possibly attributed to the covalent binding to MoS$_2$. I-Ph-MoS$_2$ exhibits three major Raman active modes at 1056, 1182, and 1540 cm^{-1} (Figure S12, Supporting Information). The latter two agree relatively well with the experimentally detected peaks of fun-MoS$_2$ (1168 and 1528 cm^{-1} in Table S2 (Supporting Information), laser power = 2.5 mW), confirming the presence of the iodophenyl functional group in our fun-MoS$_2$ samples. All three modes are also present and Raman active in the other two motifs (BPh-2MoS$_2$ and OH-Ph-MoS$_2$), in which the frequencies are slightly shifted (for

more details, see Figures S14 and S15, respectively, Supporting Information).

However, in contrast to I-Ph-MoS_2 there is one more strong Raman active mode occurring at 1276 and 1260 cm^{-1} for BPh-2MoS_2 and OH-Ph-MoS_2, respectively. This mode is in good agreement with the experimentally measured peaks of fun-MoS_2 at 1241, 1246, and 1246 cm^{-1} for lower laser powers of 0.2, 2.5, and 5.4 mW, respectively (Table S3, Supporting Information). The presence of this additional Raman mode suggests the proposed photochemical deiodination and the formation of BPh-2MoS_2 and OH-Ph-MoS_2. The Raman active modes of I-Ph-MoS_2, BPh-2MoS_2, and OH-Ph-MoS_2 overlap significantly, making it difficult to distinguish their individual contributions. However, we believe that prior to the laser writing process, the photolabile iodophenyl groups are the dominant functional groups in the deposited fun-MoS_2 LB layer. Our previous study[9] demonstrated that laser irradiation of a material stack containing functionalized MoS_2 (bearing photo-inert substituted phenyl groups) and graphene resulted in minimal changes in the 2D-band intensity and no functionalization of graphene, which contrasts with the findings of this work. Most importantly, the correlation between DFT-simulated and experimentally observed Raman peaks supports the formation of surface-tethered phenol and biphenyl motifs in fun-MoS_2 following laser irradiation.

3. Conclusion

In summary, we have demonstrated a laser-writing strategy to create patterned TMD/G heterostructures efficiently. By selectively irradiating the fun-TMD/G heterostructures with a laser, we initiated local reactions of the photolabile ends of the surface-tethered functional groups in the fun-TMDs along the laser-written paths. This process led to the formation of chemically modified domains with distinct optical and electronic properties. These domains were characterized using Raman, KPFM, XPS, and ToF-SIMS techniques, along with DFT simulations, revealing laser-induced cross-coupling between the phenyl functional groups on MoS_2 and the graphene bottom layer. Furthermore, the analysis emphasizes the potential of laser-induced dimerization and oxidation of surface-tethered phenyl moieties at the interfaces of TMD nanosheet networks, providing deeper insight into their structural evolution and interfacial interactions. These chemical insights enhance the understanding of the interface structures and properties of exfoliated TMD networks, while also highlighting the potential to customize interlamellar gaps and properties in 2D heterostructures through spatially defined, laser-triggered reactions. Our work marks a significant step in the scalable production of 2D heterostructures using functionalized 2D material inks. The TMD inks demonstrated here can be extended to other functionalized 2D materials, thanks to advances in the functionalization of 2D materials in solution. By combining solution-processed inks with advanced deposition and laser-based techniques, our method offers a promising pathway for the programmable and efficient printing of functional heterostructures. This progress opens up the possibility for mass production of heterostructure-based devices, with potential applications across various fields, including flexible electronics, sensors, and optoelectronics.

4. Experimental Section

Material Preparation Methods—Chemicals: MoS_2, $MoSe_2$, and WS_2 powders were purchased from Sigma–Aldrich and dried at 80 °C overnight under vacuum before use. *n*-Hexane (anhydrous, 95%), *n*-butyllithium (2.0 M) in cyclohexane, cyclohexane, ethanol, isopropanol (IPA), and toluene were purchased from Sigma–Aldrich and used as received. Monolayer trivial transfer G (10 mm × 10 mm) covered by poly (methyl methacrylate) (PMMA) was purchased from ACS material.

Material Preparation Methods—Synthesis of 4-Iodobenzenediazonium Tetrafluoroborate: A solution of fluoroboric acid (3.00 mL, 17.0 mmol, 1.70 equiv.) was added to a solution of 4-iodoaniline (2.19 g, 10.0 mmol, 1.00 equiv.) in H_2O (3.00 mL). The mixture was cooled down to 0 °C. Then an ice-cold solution of sodium nitrite in distilled water (3.00 mL, 10.2 mmol, 1.02 equiv.) was slowly added into the above mixture and stirred at 0 °C for 0.5 h. The precipitate was collected through filtration and washed with 1–2 mL cold water. The solid was re-dissolved into the minimum amount of acetone, and then white crystals were crashed out by gradual addition of diethyl ether. The resulting purified product was obtained in 65% yield (2.05 g, 6.44 mmol). ^{1}H NMR (400 MHz, DMSO) δ = 8.40 (d, J = 9.0 Hz, 2H), 8.32 (d, J = 9.0 Hz, 2H), 2.47 (p, J = 1.9 Hz, 4H) ppm.

Material Preparation Methods—Preparation of ce-TMD Nanosheets (TMD = MoS_2, WS_2, and $MoSe_2$): Inside a glovebox (<0.1 ppm O_2 and H_2O), 300 mg pre-dried TMD powder was added to *n*-butyllithium (2.0 M in cyclohexane, 3 mL), and the mixture was stirred at room-temperature for 4 to 5 days. Then, the reaction mixture was taken out of the glovebox and diluted with anhydrous *n*-hexane (6 mL). Subsequently, the diluted reaction mixture was added dropwise to de-ionized water (200 mL) at 0 °C to form a black dispersion. After the gas generation stopped, the organic impurities were removed by extraction with cyclohexane (200 mL), and the aqueous phase was collected in a Duran bottle and deaerated under Argon flow for 15 min. The resulting aqueous dispersion was sealed and subjected to bath-sonication (Bandelin, Sonorex DigiPlus, DL 255 H, 35 kHz) at room-temperature for 1 h and then subjected to centrifugation at 750 rpm (630 g, Sigma 3–30 K centrifuge equipped with a fixed angle rotor 12 159) at 15 °C for 1 h to remove the heavier non-exfoliated TMD flakes in the sediment. The exfoliated material in the supernatant was collected and thoroughly washed with de-ionized water three times through high-speed centrifugation at 13 000 rpm (189 280 g, 1 h, 15 °C) to remove very small flakes of TMDs and lithium hydroxide (LiOH) in the supernatant. The sediment after all washing steps was re-dispersed in de-ionized water for further functionalization and characterization.

Material Preparation Methods—Preparation of Functionalized TMD Inks: To 60 mL of ce-TMD (C[MoS_2] = 0.759 mg mL^{-1}, C[WS_2] = 0.55 mg mL^{-1}, and C[$MoSe_2$] = 1.13 mg mL^{-1}) aqueous dispersion, 30 mL of the pre-dissolved 4-iodobenzenediazonium tetrafluoroborate aqueous solution (10 equiv.) was added dropwise. The mixture was allowed to stir at room-temperature overnight. The resulting precipitate was collected by vacuum filtration using a cellulose filter membrane (0.2 µm, Sartorius), washed thoroughly with ethanol, IPA, and de-ionized water (twice for each) until the filtrate became colourless. The purified material was dried under vacuum overnight, and weighted as the intermediate product fun-TMDs, which was then redispersed in water or IPA as functionalized fun-TMD inks for the following steps.

Material Preparation Methods—Preparation of Fun-TMD/G Stacks: The fun-TMD/G stacks were prepared in two major steps: 1) deposition of the G bottom layer, 2) deposition of fun-TMDs. (1) The trivial transfer G film was transferred onto the surface of water and then fished carefully onto a Si/SiO_2 wafer. The G@Si/SiO_2 was dried at room-temperature for 30 min and then at 100 °C for ≈15 min to remove adsorbed or encapsulated water. Then G on a Si/SiO_2 substrate was immersed into preheated acetone (50 °C) for ≈30 min to remove the PMMA layer, and then dried at 50 °C for 10 min for the following steps. 2) To deposit the fun-TMD layer on top of the G film, fun-TMD inks were first re-dispersed in IPA and then slowly dropped into the mixture of water and toluene (v/v = 24/1). After 5 min, a thin and relatively uniform yellowish layer was formed. After the

evaporation of toluene, this assembled fun-TMD layer was fished onto the pre-prepared G@Si/SiO_2 and dried at room-temperature overnight.

Instrumentation and Characterization Methods—Raman Spectroscopy: Laser power-dependent Raman measurements were performed on a Horiba Jobin Yvon LabRAM Aramis confocal Raman microscope with a 532 nm excitation laser (size of laser spot ≈1 µm) under ambient conditions. The Raman emission was collected by a 50× objective (Olympus LMPlanF1 50×, numerical aperture (NA) = 0.5) and dispersed by a 600 lines mm^{-1} grating. The spectrometer was calibrated in frequency using a standard silicon wafer. The mean spectrum of 25 measured Raman single-point spectra from a 5 × 5 μm^2 map was displayed. Direct laser patterning (laser writing/reading process) was performed using a WiTec alpha300 R confocal Raman imaging microscope. The system was equipped with a motorized XYZ stage (with minimum step sizes of 10 nm in XY and 30 nm in Z) and a high-sensitivity charge coupled device (CCD) detector (1024 × 128 pixels, cooled to −65 °C, capable of acquiring 80 spectra per second). Measurements were recorded using a 532 nm green laser (with a Gaussian spot profile and a spot size of ≈350 nm), along with a 600 grooves mm^{-1} grating and a 100× Zeiss EC "Epiplan-Neofluar" differential interference contrast (DIC) objective (NA = 0.90, 0.26 mm working distance). The diffraction-limited lateral resolution was ≈200 nm, with a focal depth of ≈1 µm. The spectrometer was calibrated in frequency using a standard silicon wafer. During the laser writing process, chemically modified domains were created using a 532 nm laser with power settings of 12, 15, and 17 mW for fun-MoS_2/G, fun-WS_2/G, and fun-$MoSe_2$/G, respectively, with an integration time of 1 s. For the reading process, a laser power of 2 or 7 mW was used, also with an integration time of 1 s.

Instrumentation and Characterization Methods—Zeta Potential: Zeta potential (ζ) measurements were performed using a Malvern Zetasizer Nano ZEN3600 system with a 633 nm He-Ne laser. Samples (aqueous dispersions) were loaded into folded capillary cells (DTS1070), and electrophoretic mobility (µ) was determined using a combination of electrophoresis and laser Doppler velocimetry. The zeta potential ζ was calculated from the measured mobility µ using the Smoluchowski approximation. The displayed values represent the mean of five measurements. All measurements were conducted at 25 °C.

Instrumentation and Characterization Methods—Thermogravimetric Analysis (TGA): TGA measurements were carried out on a Netzsch STA 409 CD instrument with the following programmed time-dependent temperature profile: 30–700 °C with 10 K min^{-1} gradient. The initial sample weights were ≈3–5 mg, and the experiments were performed under an inert gas atmosphere with a Helium gas flow of 80 mL min^{-1}.

Instrumentation and Characterization Methods—X-ray Photoelectron Spectroscopy (XPS): XPS was performed on a Specs EnviroESCA spectrometer in ultrahigh vacuum at a pressure of less than 10^{-7} mbar using a monochromated Al Kα X-ray source (1486.6 eV) at a source-to-sample angle of 55°. For the measurements, the sample material was deposited on a 300 nm SiO_2/Si wafer, and the binding scale was referenced to the carbon 1s nuclear level at 284.4 eV. For the survey spectra, the 700–50 eV range was analyzed with a pass energy of 100 eV and a 0.2 s dwell time. For the HR (high resolution) spectra, 5 to 15 spectra were collected with a reduced pass energy of 15 eV and the same dwell time. The resulting spectra were processed by UniFIT with Gaussian-Lorentzian line shapes (50-50).

Instrumentation and Characterization Methods—Time-of-Flight Secondary Ion Mass Spectrometry (ToF-SIMS): ToF-SIMS analysis was performed using a ToF-SIMS MVI instrument (IONTOF GmbH, Münster, Germany). The samples were analyzed at room-temperature. Measurements were conducted in collimated burst alignment mode with a 30 keV Bi_3^+ primary ion beam in positive polarity with a beam current of 0.69 pA. A field of view (FoV) measuring 200 × 200 µm was rastered in random mode with 512 × 512 pixels, acquiring one shot per pixel. Spectra were calibrated using typical organic fragments (CH_2^+at 14.02, $C_2H_4^+$ at 28.03, $C_3H_6^+$ at 42.05, $C_4H_8^+$ at 56.06).

Instrumentation and Characterization Methods—Atomic force microscopy (AFM) and Kelvin Probe Force Microscopy (KPFM): AFM was carried out using a Bruker Dimension Icon microscope. Bruker Scanasyst-Air silicon tips on nitride levers with a spring constant of 0.4 N m^{-1} were used to obtain images resolved by 1024 × 1024 pixels. The KPFM measurement was performed under ambient conditions with non-contact mode (AFM tip: SCM-PIT-v2, platinum-iridium coated). Amplitude-modulated KPFM in a dual pass configuration was used. In the first scan the topography was received and in the second pass the potential profile was measured while keeping the tip at a constant distance (100 nm) from the sample surface.

Density Functional Theory (DFT): The density functional theory (DFT) calculations were performed using the quantum espresso suite.[25,26] The unit cells for the fun-MoS_2 calculations comprise a biphenyl molecule sandwiched between two MoS_2 layers, each with a 2 × 2 supercell. To avoid unwanted interactions between structures of neighboring cells the size of the unit cell in the direction perpendicular to the MoS_2 layers was set to 45 Å. Ultrasoft pseudopotentials provided by the GBRV library[27] were used for the relaxation and phonon calculations, employing the PBE exchange-correlation functional.[28] k points were sampled on a 8 × 8 × 1 Monkhorst-Pack grid. A converged plane wave cutoff of 80 Ry (1088.46 eV) was used. The unit cell lattice vectors (except for the lattice vector in the direction perpendicular to the MoS_2 layers) were allowed to change during the relaxation process, which was performed until the forces on each atom were less than 0.005 eV $Å^{-1}$.

All calculations of further structures in which biphenyl was replaced by other functional groups, i.e., iodophenyl, phenol, or just one phenyl ring sandwiched between two MoS_2 layers or functionalized on one MoS_2 layer, were performed accordingly. For the calculation of the Raman intensities of iodophenyl, biphenyl, and phenol, I-Ph-2MoS_2, BPh-2MoS_2, and OH-Ph-2MoS_2 were relaxed again using norm-conserving pseudopotentials from the SPMS library,[29] which are required for such calculations. For these calculations the local density approximation (LDA) was used for the exchange-correlation functional, since it is well suited for phonon calculations. Convergence tests show that the previously employed parameters were still sufficient. To keep the computational cost to a minimum, the MoS_2 layers were removed, and the molecules were allowed to relax again. This time the unit cell was not allowed to change to maintain the dimensions provided by the constraining MoS_2 layers. The resulting related vibrational modes were ≈30–40 cm^{-1} lower in the relevant areas. These deviations may be caused by the presence of the MoS_2 layers. Slight differences could also arise from the use of different pseudopotentials and approximations for the calculations in question. The qualitative results are in good agreement with the previously calculated respective phonon modes. Images created using XCrysDen.[30]

Statistical Analysis: Each Raman spectrum was the mean spectrum of 25 single-point Raman measurements taken from a 5 × 5 μm^2 map. In the stacked layout of Raman spectra, all spectra from MoS_2- and WS_2-containing samples were normalized to the intensity of the E^1_{2g} mode for comparison, while those from $MoSe_2$-containing samples were normalized to the A_{1g} mode. For the statistical analysis of Raman peak position, FWHM, and intensity, the spectra were fitted using a Lorentzian function. The extracted values, including peak position, FWHM, and intensity, were shown with standard errors represented by the scale bars. Statistical analysis was performed using Origin software.

Supporting Information

Supporting Information is available from the Wiley Online Library or from the author.

Acknowledgements

X.C. and S.W. contributed equally to this work. This project has received funding from the European Union's Horizon 2020 research and innovation programme Graphene Flagship under grant agreement No 881603 and Emerging Talents Initiative (FAUeti) funded by Friedrich-Alexander-Universität Erlangen-Nürnberg (FAU). The authors would like to acknowledge the research infrastructure and support provided by the SupraFAB research building realized with funds from the Federal Government and the State of Berlin and the assistance of the Core Facility

BioSupraMol supported by the DFG. The authors gratefully acknowledge the scientific support and HPC resources provided by the Erlangen National High Performance Computing Center (NHR@FAU) of the Friedrich-Alexander-Universität Erlangen-Nürnberg (FAU) under the NHR project b181dc. NHR funding is provided by federal and Bavarian state authorities. NHR@FAU hardware is partially funded by the German Research Foundation (DFG) – 440719683. [Correction added on June 11, 2025, after first online publication: A typo error in equation (2) has been corrected in this version.]

Open access funding enabled and organized by Projekt DEAL.

Conflict of Interest

The authors declare no conflict of interest.

Data Availability Statement

The data that support the findings of this study are available from the corresponding author upon reasonable request.

Keywords

2D heterostructures, interface engineering, laser writing, patterning, transition metal dichalcogenides

Received: February 19, 2025
Revised: April 8, 2025
Published online:

[1] S. Gbadamasi, M. Mohiuddin, V. Krishnamurthi, R. Verma, M. W. Khan, S. Pathak, K. Kalantar-Zadeh, N. Mahmood, *Chem. Soc. Rev.* **2021**, *50*, 4684.
[2] J. Shi, R. Tong, X. Zhou, Y. Gong, Z. Zhang, Q. Ji, Y. Zhang, Q. Fang, L. Gu, X. Wang, Z. Liu, Y. Zhang, *Adv. Mater.* **2016**, *28*, 10664.
[3] L. Yuan, B. Zheng, J. Kunstmann, T. Brumme, A. B. Kuc, C. Ma, S. Deng, D. Blach, A. Pan, L. Huang, *Nat. Mater.* **2020**, *19*, 617.
[4] Y. Liu, Y. Huang, X. Duan, *Nature* **2019**, *567*, 323.
[5] K. S. Novoselov, A. Mishchenko, A. Carvalho, A. H. Castro Neto, *Science* **2016**, *353*, aac9439.
[6] S. Ippolito, A. G. Kelly, R. Furlan de Oliveira, M. A. Stoeckel, D. Iglesias, A. Roy, C. Downing, Z. Bian, L. Lombardi, Y. A. Samad, V. Nicolosi, A. C. Ferrari, J. N. Coleman, P. Samorì, *Nat. Nanotechnol.* **2021**, *16*, 592.
[7] A. D. Sinnott, A. Kelly, C. Gabbett, J. Munuera, L. Doolan, M. Mobius, S. Ippolito, P. Samorí, J. Coleman, G. L. W. Cross, *Adv. Mater.* **2023**, *36*, 2306954.
[8] M. Vázquez Sulleiro, A. Develioglu, R. Quirós-Ovies, L. Martín-Pérez, N. Martín Sabanés, M. L. Gonzalez-Juarez, I. J. Gómez, M. Vera-Hidalgo, V. Sebastián, J. Santamaría, E. Burzurí, E. M. Pérez, *Nat. Chem.* **2022**, *14*, 695.
[9] X. Chen, M. Assebban, M. Kohring, L. Bao, H. B. Weber, K. C. Knirsch, A. Hirsch, *J. Am. Chem. Soc.* **2022**, *144*, 9645.
[10] T. Pinheiro, M. Morais, S. Silvestre, E. Carlos, J. Coelho, H. V. Almeida, P. Barquinha, E. Fortunato, R. Martins, *Adv. Mater.* **2024**, *36*, 2402014.
[11] X. Chen, C. Bartlam, V. Lloret, N. Moses Badlyan, S. Wolff, R. Gillen, T. Stimpel-Lindner, J. Maultzsch, G. S. Duesberg, K. C. Knirsch, A. Hirsch, *Angew. Chem., Int. Ed.* **2021**, *60*, 13484.
[12] K. Lee, B. M. Szydłowska, O. Hartwig, K. Synnatschke, B. Tywoniuk, T. Hartman, T. Tomašević-Ilić, C. P. Gabbett, J. N. Coleman, Z. Sofer, M. Spasenović, C. Backes, G. S. Duesberg, *J. Mater. Chem. C* **2023**, *11*, 593.
[13] E. Er, H. L. Hou, A. Criado, J. Langer, M. Möller, N. Erk, L. M. Liz-Marzán, M. Prato, *Chem. Mater.* **2019**, *31*, 5725.
[14] G. Bottari, M. Á. Herranz, L. Wibmer, M. Volland, L. Rodríguez-Pérez, D. M. Guldi, A. Hirsch, N. Martín, F. D'Souza, T. Torres, *Chem. Soc. Rev.* **2017**, *46*, 4464.
[15] Y. Bleu, F. Bourquard, A. S. Loir, V. Barnier, F. Garrelie, C. Donnet, *J. Raman Spectrosc.* **2019**, *50*, 1630.
[16] L. Bao, B. Zhao, V. Lloret, M. Halik, F. Hauke, A. Hirsch, *Angew. Chem., Int. Ed.* **2020**, *59*, 6700.
[17] A. C. Ferrari, *Solid State Commun.* **2007**, *143*, 47.
[18] Z. Peng, Z. Yan, Z. Sun, J. M. Tour, *ACS Nano* **2011**, *5*, 8241.
[19] N. Moses Badlyan, N. Pettinger, N. Enderlein, R. Gillen, X. Chen, W. Zhang, K. C. Knirsch, A. Hirsch, *Phys. Rev. B* **2022**, *106*, 104103.
[20] L. H. Grey, H. Y. Nie, M. C. Biesinger, *Appl. Surf. Sci.* **2024**, *653*, 159319.
[21] T. Matsuura, K. Omura, *Bull. Chem. Soc. Jpn.* **2006**, *39*, 944.
[22] J. Lan, R. Chen, F. Duo, M. Hu, X. Lu, *Molecules* **2022**, *27*, 5364.
[23] X. W. Huang, J. J. Wei, T. Liu, X. L. Zhang, S. M. Bai, H. H. Yang, *Nanoscale* **2017**, *9*, 17193.
[24] J. P. Perdew, K. Burke, M. Ernzerhof, *Phys. Rev. Lett.* **1996**, *77*, 3865.
[25] P. Giannozzi, S. Baroni, N. Bonini, M. Calandra, R. Car, C. Cavazzoni, D. Ceresoli, G. L. Chiarotti, M. Cococcioni, I. Dabo, A. Dal Corso, S. de Gironcoli, S. Fabris, G. Fratesi, R. Gebauer, U. Gerstmann, C. Gougoussis, A. Kokalj, M. Lazzeri, L. Martin-Samos, N. Marzari, F. Mauri, R. Mazzarello, S. Paolini, A. Pasquarello, L. Paulatto, C. Sbraccia, S. Scandolo, G. Sclauzero, A. P. Seitsonen, et al., *J. Phys.: Condens. Matter* **2009**, *21*, 395502.
[26] P. Giannozzi, O. Andreussi, T. Brumme, O. Bunau, M. Buongiorno Nardelli, M. Calandra, R. Car, C. Cavazzoni, D. Ceresoli, M. Cococcioni, N. Colonna, I. Carnimeo, A. Dal Corso, S. de Gironcoli, P. Delugas, R. A. DiStasio, A. Ferretti, A. Floris, G. Fratesi, G. Fugallo, R. Gebauer, U. Gerstmann, F. Giustino, T. Gorni, J. Jia, M. Kawamura, H. Y. Ko, A. Kokalj, E. Küçükbenli, M. Lazzeri, et al., *J. Phys.: Condens. Matter* **2017**, *29*, 465901.
[27] K. F. Garrity, J. W. Bennett, K. M. Rabe, D. Vanderbilt, *Comput. Mater. Sci.* **2014**, *81*, 446.
[28] A. Grozin, *Comput. Phys. Commun.* **2023**, *283*, 108590.
[29] M. F. Shojaei, J. E. Pask, A. J. Medford, P. Suryanarayana, *Comput. Phys. Commun.* **2023**, *283*, 108594.
[30] A. Kokalj, *J. Mol. Graphics Model.* **1999**, *17*, 176.